Differentiation of Solid Renal Tumors with Multiparametric MR Imaging[1]

Camila Lopes Vendrami, MD
Carolina Parada Villavicencio, MD
Todd J. DeJulio, MD
Argha Chatterjee, MD
David D. Casalino, MD
Jeanne M. Horowitz, MD
Daniel T. Oberlin, MD
Guang-Yu Yang, MD
Paul Nikolaidis, MD
Frank H. Miller, MD

[1]From the Departments of Radiology (C.L.V., C.P.V., A.C., D.D.C., J.M.H., P.N., F.H.M.), Pathology (T.J.D., G.Y.Y.), and Urology (D.T.O.), Northwestern Memorial Hospital, Northwestern University Feinberg School of Medicine, 676 N St Clair St, Suite 800, Chicago, IL 60611. Recipient of a Cum Laude award for an education exhibit at the 2016 RSNA Annual Meeting. Received March 6, 2017; revision requested May 18 and received June 9; accepted June 30. For this journal-based SA-CME activity, the authors, editor, and reviewers have disclosed no relevant relationships. **Address correspondence to** F.H.M. (e-mail: *fmiller@northwestern.edu*).

SA-CME LEARNING OBJECTIVES

After completing this journal-based SA-CME activity, participants will be able to:

■ Discuss a clear diagnostic approach for solid renal masses using multiparametric MR imaging.

■ Identify and describe the spectrum of radiologic findings of the most common solid renal masses.

■ Illustrate imaging and pathology correlates of the most common solid renal masses.

See www.rsna.org/education/search/RG.

Characterization of renal tumors is critical to determine the best therapeutic approach and improve overall patient survival. Because of increased use of high-resolution cross-sectional imaging in clinical practice, renal masses are being discovered with increased frequency. As a result, accurate imaging characterization of these lesions is more important than ever. However, because of the wide array of imaging features encountered as well as overlapping characteristics, identifying reliable imaging criteria for differentiating malignant from benign renal masses remains a challenge. Multiparametric magnetic resonance (MR) imaging based on various anatomic and functional parameters has an important role and adds diagnostic value in detection and characterization of renal masses. MR imaging may allow distinction of benign solid renal masses from several renal cell carcinoma (RCC) subtypes, potentially suggest the histologic grade of a neoplasm, and play an important role in ensuring appropriate patient management to avoid unnecessary surgery or other interventions. It is also a useful noninvasive imaging tool for patients who undergo active surveillance of renal masses and for follow-up after treatment of a renal mass. The purpose of this article is to review the characteristic MR imaging features of RCC and common benign renal masses and propose a diagnostic imaging approach to evaluation of solid renal masses using multiparametric MR imaging.

©RSNA, 2017 • radiographics.rsna.org

Introduction

Recently, as a result of increased use of high-resolution cross-sectional imaging, the number of incidental solid renal masses has increased, requiring further imaging characterization for proper diagnosis (1). This characterization extends beyond the simple determination of malignancy and benignity, as it determines and guides the therapeutic approach and follow-up management (2). In the past, a solid enhancing mass in the kidney was considered renal cell carcinoma (RCC) with no need for further characterization, as these were invariably resected. However, with time, advances in the understanding and treatment of renal masses have occurred and led to the discovery of an increasingly complex range of tumor subtypes (3).

In addition to enabling proper characterization of solid renal lesions, cross-sectional imaging is also necessary for staging purposes in patients with known disease, for assessment of recurrence in patients with previously treated disease, and for active surveillance in high-risk patients. RCC is one of the most frequently diagnosed adult cancers,

RadioGraphics

TEACHING POINTS

- At MR imaging, clear cell carcinomas typically show high T2 signal intensity and a tendency to be heterogeneous because of necrosis, cystic degeneration, and/or hemorrhage. On T1-weighted images, clear cell RCC shows low signal intensity to similar signal intensity to that of the renal parenchyma. They are hypervascular tumors, often showing heterogeneous enhancement after contrast material administration during the arterial phase and enhancing more avidly than the other RCCs, a feature helpful in distinction between subtypes of RCC. Differentiating clear cell RCCs from hypervascular benign masses such as oncocytomas and AMLs remains a challenge. Another recognized feature in 60% of clear cell carcinomas is the presence of intralesional microscopic fat, which may appear as a drop in signal intensity on opposed-phase chemical shift images relative to that on in-phase images; greater than 25% signal loss may be predictive.

- Papillary RCCs usually demonstrate low T2 signal intensity and are hypovascular with progressive enhancement after contrast material administration. They may contain hemosiderin, leading to areas with signal loss on in-phase images relative to opposed-phase images at chemical shift imaging.

- Chromophobe RCCs share the same origin as oncocytomas and have overlapping histologic and imaging features.

- At MR imaging, classic AMLs demonstrate high T1 signal intensity because of their fat content. The presence of macroscopic fat can be appreciated as suppression of signal intensity on frequency-selective fat-saturated images and as india ink artifact on opposed-phase images.

- At MR imaging, these lesions are homogeneous and show low signal intensity on T2-weighted images due to the presence of abundant smooth muscle and high signal intensity on T1-weighted images. The enhancement pattern of lipid-poor AMLs is typically early intense enhancement with subsequent washout, although it can be variable. Lipid-poor AMLs may appear as an exophytic non-round lesion without a capsule. Lipid-poor AMLs may show a drop in signal intensity on opposed-phase images when compared with in-phase images.

accounting for 2%–3% of all adult malignancies (4). The most common RCC subtypes, which are associated with distinct biologic behavior, prognosis, and therapeutic approach, include clear cell, papillary, and chromophobe tumors (5).

Because of the heterogeneity of imaging features as well as overlapping imaging characteristics, the lack of reliable imaging criteria for recognition of malignant versus benign masses remains a challenge. Several imaging parameters have been proposed to distinguish the different renal lesions. There are two main benign lesions that may be difficult to differentiate from RCC. These are angiomyolipomas (AMLs), in particular the lipid-poor subtype, which are overall the most common benign solid renal neoplasm, and oncocytomas, which represent 3%–7% of all renal tumors (6,7).

Magnetic resonance (MR) imaging is a useful noninvasive imaging tool for diagnosis and characterization of renal lesions because it provides excellent soft-tissue contrast and functional information. Renal multiparametric MR imaging

allows characterization of lesion vascularity and diffusion restriction and may allow differentiation of malignant from benign lesions. In addition, multiparametric MR imaging may aid in classifying RCC subtypes and histologic grades (8).

In this article, we review and evaluate the diagnostic value that a multiparametric MR imaging approach adds to identification and differentiation of the most common types of solid renal masses, including RCC subtypes, AML, and oncocytoma. The classic MR imaging features of these solid renal lesions are also discussed and illustrated.

Imaging Protocol

The multiparametric MR imaging protocol for evaluation of renal masses at our institution includes T2-weighted sequences, chemical shift imaging (in-phase and opposed-phase), fat-suppressed T1-weighted sequences before and after administration of gadolinium contrast material, diffusion-weighted imaging (DWI), and dynamic contrast-enhanced sequences (Table 1).

Contrast material injections at our institution are performed with (a) gadobenate dimeglumine (MultiHance; Bracco Diagnostics, Milan, Italy) at a dose of 0.05 mmol/kg in patients with a glomerular filtration rate of 30–60 mL/min/1.73 m^2 because of higher relaxivity or with (b) gadobutrol (Gadovist; Bayer Healthcare Pharmaceuticals, Berlin, Germany) at a dose of 0.1 mmol/kg in patients with a glomerular filtration rate greater than 60 mL/min/1.73 m^2, followed by a 20-mL saline flush (2 mL/sec) with a power injector (Spectris; Medrad, Warrendale, Pa).

Renal Cell Carcinoma

RCC is the most common malignant epithelial tumor, accounting for approximately 90% of all solid renal tumors in adults (4). RCC comprises a heterogeneous group of tumors with varying prognosis, response to treatment, histologic and imaging findings, biologic behavior, and cytogenetic abnormalities (Table 2) (5,9,10). Generally, the median age at diagnosis is 65 years with a predominance of male patients (4). The three main histologic subtypes of RCC are clear cell, papillary, and chromophobe tumors.

Clear Cell RCC

Clear cell RCC is the most common subtype of RCC, accounting for 65%–80% of cases (5,8). It is mostly sporadic in 95% of the cases; the remaining 5% are associated with hereditary syndromes including von Hippel–Lindau disease and tuberous sclerosis (11). Clear cell carcinomas are associated with a less favorable outcome than the other two RCC subtypes, with a 5-year survival rate of 44%–69% (5,12). Sarcomatoid differentiation and

Table 1: Multiparametric MR Imaging Protocol for Evaluation of Renal Masses

Sequences	Imaging Planes
T1-weighted dual-echo in-phase/opposed-phase GRE	Axial
3D fat-saturated SPGR T1-weighted (nonenhanced and gadolinium-enhanced DCE sequences: corticomedullary, nephrographic, and excretory phases)*	Axial, coronal, and/or sagittal
T2-weighted HASTE	Axial and coronal and/or sagittal
T2-weighted TSE with fat suppression	Axial
Spin-echo EPI DWI (b = 50, 500, and 800 sec/mm^2) + ADC map	Axial

Note.—ADC = apparent diffusion coefficient, DCE = dynamic contrast-enhanced, EPI = echo-planar imaging, GRE = gradient-echo, HASTE = half-Fourier acquisition single-shot turbo spin-echo, SPGR = spoiled gradient-echo, 3D = three-dimensional, TSE = turbo spin-echo.
*Corticomedullary phase images were obtained at approximately 40 seconds after contrast material administration using "fluoro-prep" timing, with nephrographic phase images obtained at 90 seconds and excretory phase images at 3 minutes.

Table 2: Characteristics of RCC Subtypes

RCC Subtypes	Prevalence	Origin	Distinguishing MR Imaging Features	Biologic Behavior
Clear cell	75%	Proximal nephron	High to intermediate signal intensity on T2-weighted images Microscopic fat Avid enhancement Areas of necrosis	Aggressiveness depends on Fuhrman grade, stage, and sarcomatoid transformation
Papillary	10%	Distal nephron	Low signal intensity on T2-weighted images Evidence of hemosiderin (signal loss on in-phase images) Mild enhancement Cystic change may occur	Associated with overall better prognosis than clear cell subtype
Chromophobe	5%	Distal nephron	Intermediate signal intensity on T2-weighted images Homogeneous Moderate enhancement Necrosis not common	5-year survival rate: 78%–93%

rhabdoid differentiation are rare and are each associated with a poorer prognosis (10,13).

Clear cell tumors originate from the epithelium of the proximal convoluted tubules with predominantly expansible growth (14). Macroscopically, they have a golden-yellow appearance because of their lipid-rich contents (15). Histologically, they are composed of cells with optically clear cell cytoplasm due to accumulation of cholesterol and dissolved lipids (5,16). Tumor cells are typically arranged in sheets, acini, or alveoli, and prominent thin-walled vasculature is characteristic. They often contain cells with granular eosinophilic cytoplasm (Fig 1) (5).

The most widely accepted histopathologic grading system for this RCC subtype is the Fuhrman classification grading system (17,18), which is based on nuclear size and features. It classifies clear cell carcinomas into four grades (I–IV), with grades I and II referred to as low-grade tumors and grades III and IV referred to as high-grade tumors (17,19). Higher-grade tumors are associated with a poorer prognosis (20).

At MR imaging, clear cell carcinomas typically show high T2 signal intensity and a tendency to be heterogeneous because of necrosis, cystic degeneration, and/or hemorrhage (16,21). On T1-weighted images, clear cell RCC shows low signal intensity to similar signal intensity to that of the renal parenchyma (15). They are hypervascular tumors, often showing heterogeneous enhancement after contrast material administration during the arterial phase and enhancing more avidly than the other RCCs, a feature helpful in distinction between subtypes of RCC (22,23). Differentiating clear cell RCCs
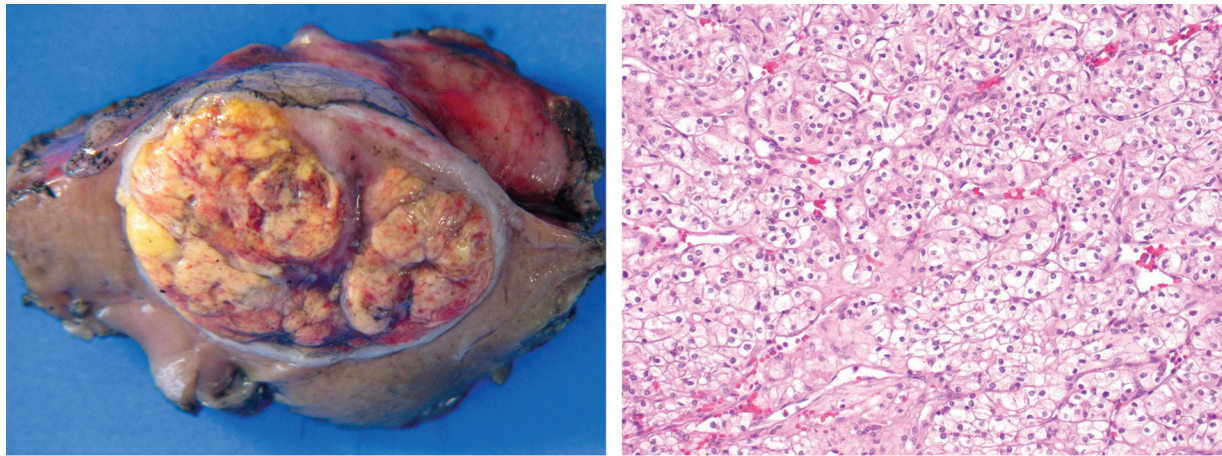
RadioGraphics

a.   b.

Figure 1.   Clear cell RCC. **(a)** Photograph of a sectioned gross specimen shows a clear cell RCC (golden-yellow appearance). **(b)** Photomicrograph shows nests of tumor cells with clear cytoplasm, round nuclei, and inconspicuous nucleoli surrounded by a fine fibrovascular network. (Hematoxylin-eosin [H-E] stain; original magnification, ×100.)

from hypervascular benign masses such as oncocytomas and AMLs remains a challenge (22).

Another recognized feature in 60% of clear cell carcinomas is the presence of intralesional microscopic fat, which may appear as a drop in signal intensity on opposed-phase chemical shift images relative to that on in-phase images; greater than 25% signal loss may be predictive (Fig 2) (16,22,24). Central necrosis is a common feature of clear cell RCCs and is seen as a homogeneous hypointense area in the center of the mass on T1-weighted images, with moderate to high signal intensity on T2-weighted images and nonenhancement after contrast material administration (11) (Fig 3). Necrosis has been shown to correlate with tumor size and grade (5,13,25).

Clear cell RCCs show a propensity to invade vessels (45% of tumors), most often the renal vein and inferior vena cava, resulting in tumor thrombosis. Therefore, evaluation of vascular involvement and extension is important (15,26). Higher tumor grade is correlated with the presence of larger size, intralesional necrosis, retroperitoneal vascular collaterals, renal vein thrombosis, and interruption of the tumor capsule (11).

A tumor pseudocapsule (or hypointense rim) may be seen on both T1- and T2-weighted images and is assumed to be related to compression of the adjacent renal parenchyma by the expanding tumor. Interruption of this pseudocapsule correlates with invasion of perirenal fat (advanced stage) and higher nuclear grade (27). It has also been reported that a decreasing trend of apparent diffusion coefficient (ADC) values is seen with increasing Fuhrman grade, suggesting that DWI may be helpful in demonstrating the aggressiveness of clear cell RCCs and predicting tumor grade (8,28,29) (Figs 2, 3).

DWI can be helpful in detecting renal masses, especially in patients who cannot receive gadolinium contrast material. The presence of restricted diffusion and lower ADC values can be seen in solid masses that are both malignant and benign, including RCC, oncocytomas, AMLs, and abscesses. Benign cystic lesions do not restrict diffusion and show higher ADC values. Clear cell tumors have been reported to have significantly higher mean ADC than non–clear cell RCCs (30–32). However, others have found no significant difference in ADC between clear cell and non–clear cell cancers (33).

Compared with papillary and chromophobe RCCs, clear cell carcinomas are more likely to be symptomatic, encountered at an advanced stage, and metastatic, accounting for 94% of metastatic RCC cases, mostly to the lungs (5,10,34,35).

Papillary RCC
Papillary carcinomas are the second most common subtype of RCC, accounting for 10%–15% of cases (5,36). They are bilateral in 4% of cases and multifocal in 23% (35). However, multifocality has been shown not to correlate with tumor type, grade, or stage (37). Papillary carcinomas generally have a better prognosis than clear cell carcinomas and a more favorable outcome, including better survival (5-year survival rate of approximately 90%) (5,35,38) and lower incidence of metastases, mostly to the lungs (34,39). Tumor epithelium is reminiscent of the epithelium of the proximal convoluted tubules (14,15).

Macroscopically, papillary RCCs often contain areas of hemorrhage, necrosis, and cystic degeneration (15). Sarcomatoid differentiation may occur in approximately 5% of cases (11). Histologically, they are composed of eosinophilic
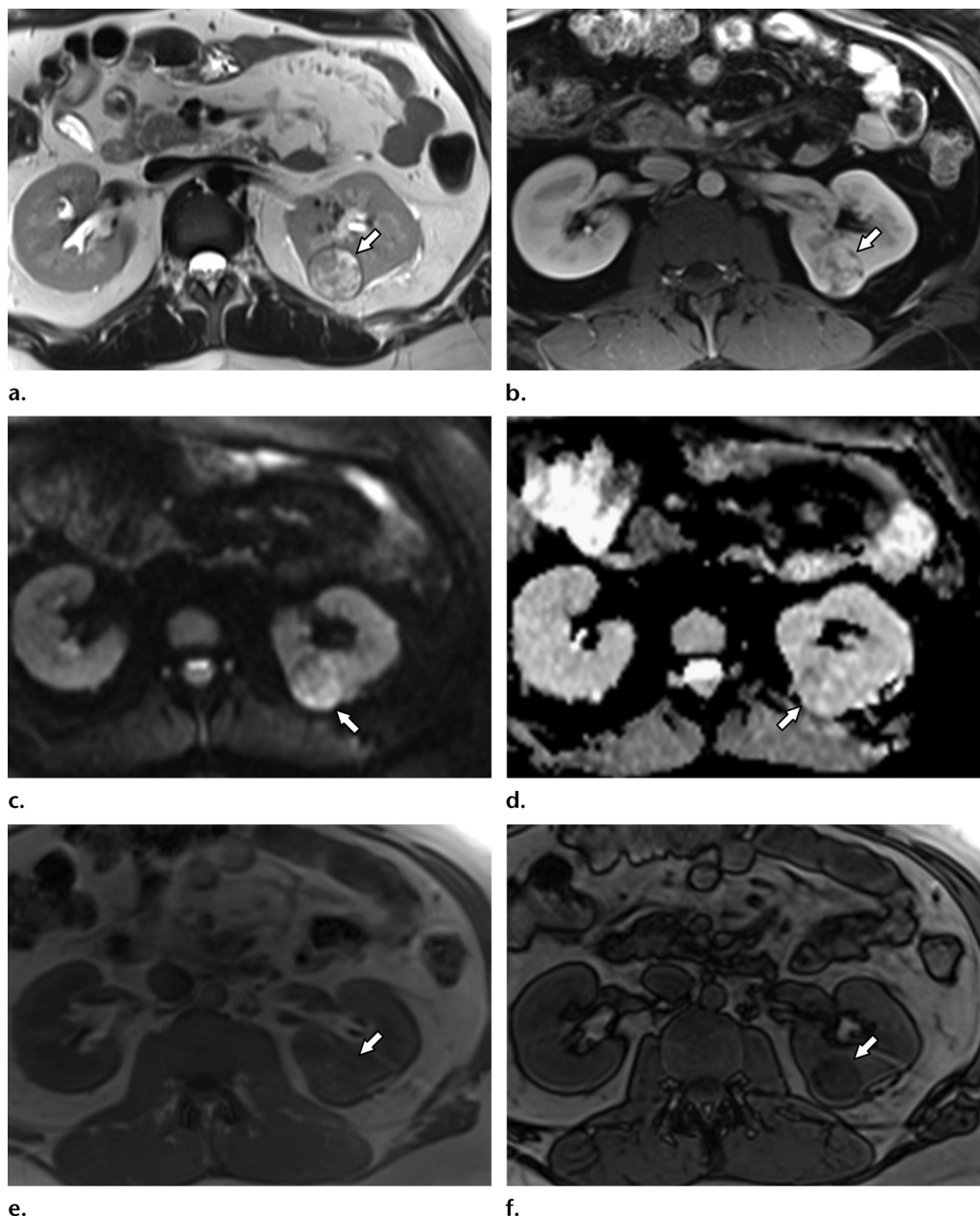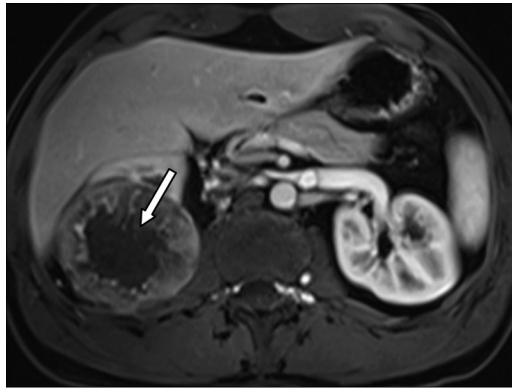
Figure 2. Low-grade clear cell RCC (Fuhrman grade II) corresponding to that in Figure 1 in a 39-year-old woman. **(a)** Axial T2-weighted MR image shows a 2.9-cm hyperintense renal mass (arrow). **(b)** Axial contrast-enhanced corticomedullary phase 3D fat-saturated SPGR T1-weighted image shows heterogeneous enhancement (arrow). **(c)** Axial diffusion-weighted image (b = 500 sec/mm^2) shows focal peripheral areas of restriction (arrow). **(d)** ADC map shows an ADC of 1.6×10^{-3} mm^2/sec (arrow). **(e, f)** Axial in-phase **(e)** and opposed-phase **(f)** T1-weighted images show a drop in signal intensity on the opposed-phase image (arrow in **f**) compared with that on the in-phase image (arrow in **e**), consistent with microscopic fat.

tumor cells with papillary growth and foamy histiocytic infiltration into the interstitium, which is laden with hemosiderin and fat (Fig 4) (38).

Papillary carcinomas have been pathologically divided by Delahunt and Eble (40) and Delahunt et al (41) into two groups: type I (basophilic), composed of small cuboidal cells with uniform nuclei covering thin papillae, and type II (eosinophilic), organized as large eosinophilic cells with pleomorphic nuclei (40–43). Both display

distinct clinical-pathologic behaviors. It has been reported that type II is associated with higher nuclear grade and pathologic stage and poorer survival rates compared with type I, which tends to be of lower Fuhrman nuclear grade (39,42).
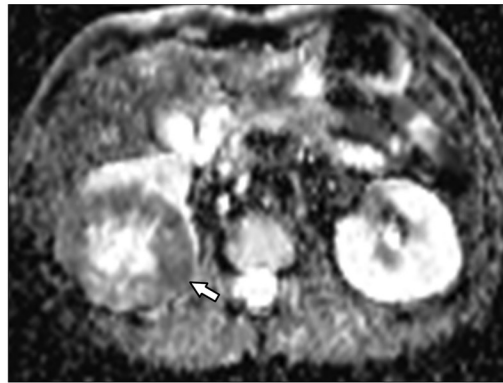
In most cases, MR imaging shows a well-circumscribed, homogeneous, peripherally located tumor that measures less than 3 cm. When tumors exceed 4 cm in diameter, internal heterogeneity may be observed because of hemorrhage,

a.
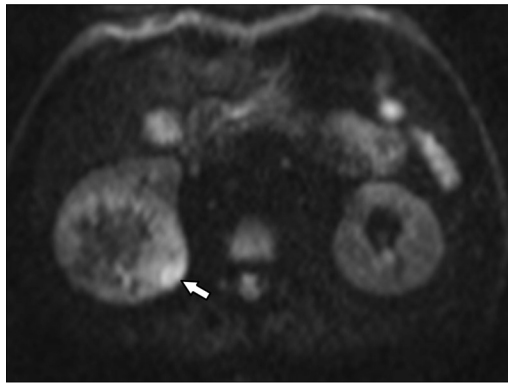
Figure 3. High-grade clear cell RCC (Fuhrman grade IV) in a 42-year-old woman. **(a)** Axial contrast-enhanced corticomedullary phase 3D fat-saturated SPGR T1-weighted image shows a heterogeneous 7.2-cm mass with a central hypointense area from cystic degeneration or necrosis (arrow). Multiple collateral vessels were seen. **(b)** Axial diffusion-weighted image ($b = 800$ sec/mm^2) shows focal peripheral areas of restriction (arrow). **(c)** ADC map shows that the peripheral portion has an ADC of 1.0 $\times$ 10^{-3} mm^2/sec (arrow). The findings of larger lesion size with central necrosis, lower ADC, and collateral vessels (not shown) favor a higher-grade tumor than that in Figure 2.

b.

c.

calcification, and necrosis (15,16). A fibrous capsule is typically present (11), with low signal intensity on T1- and T2-weighted images.

Papillary RCCs usually demonstrate low T2 signal intensity and are hypovascular with progressive enhancement after contrast material administration (2,21,43). They may contain hemosiderin, leading to areas with signal loss on in-phase images relative to opposed-phase images at chemical shift imaging (Fig 5) (15). Cystic papillary RCCs may display papillary projections, hemorrhagic fluid content, and internal mural nodules, while cystic clear cell RCCs may show clear fluid content, irregular walls, and septa (16).

The imaging appearance of papillary carcinomas differs from that of clear cell RCC, as clear cell carcinomas classically tend to have higher signal intensity on T2-weighted images, are hypervascular, and may show signal intensity drop on opposed-phase images relative to in-phase images because of the fat content. Moreover, although lipid-poor AMLs also show low signal intensity on T2-weighted images, lipid-poor AMLs tend to show avid enhancement after contrast material administration, whereas papillary RCCs are hypovascular and show progressive enhancement (8). Furthermore, for papillary RCCs, the arterial wash-in index (postcontrast arterial phase) (calculated as [$SI_{postcontrast}$ − $SI_{precon-}$

$_{trast}$]/$SI_{precontrast}$ $\times$ 100, where SI = signal intensity) has been reported to be lower than for lipid-poor AMLs, which corroborates the low enhancement of papillary tumors after contrast material administration as well as the high arterial wash-in of AMLs (2). Rarely, papillary RCC may manifest with internal foci of microscopic fat (from interstitial macrophages with cholesterol) or even intracytoplasmic fat (16).

Papillary RCCs have been reported to show lower ADCs than clear cell RCCs, although overlap exists, and other MR imaging features should be considered when differentiating them (3,32). Blood products, such as hemosiderin, show low signal intensity at DWI because of magnetic susceptibility effects; therefore, ADCs cannot be reliably calculated for hemorrhage products because they have very low signal intensity on T2-weighted images (44).

Chromophobe RCC

Chromophobe carcinomas account for 4%–11% of RCCs and are the third most common subtype (5,11). These tumors have generally been associated with a better prognosis than clear cell RCCs, with a 5-year survival rate of approximately 78%–93% (45,46); however, there is ongoing investigation as to the prognosis of chromophobe carcinomas as well as the significance of some

Figure 4. Papillary RCC. **(a)** Photograph of a sectioned gross specimen shows a papillary RCC with hemorrhage and necrosis (arrows). **(b)** High-power photomicrograph shows papillae lined by cells with scant cytoplasm, some with intracellular hemosiderin (arrowheads) and some with foamy macrophages (arrow). (H-E stain; original magnification, ×100.) **(c)** High-power photomicrograph shows concentric microcalcifications filling the cores of the papillae (psammoma bodies) (arrows). (H-E stain; original magnification, ×100.)
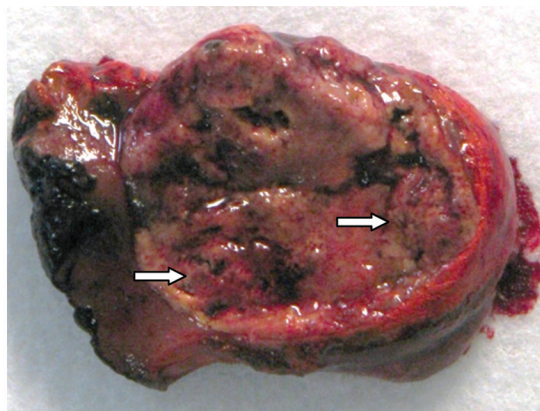
a.
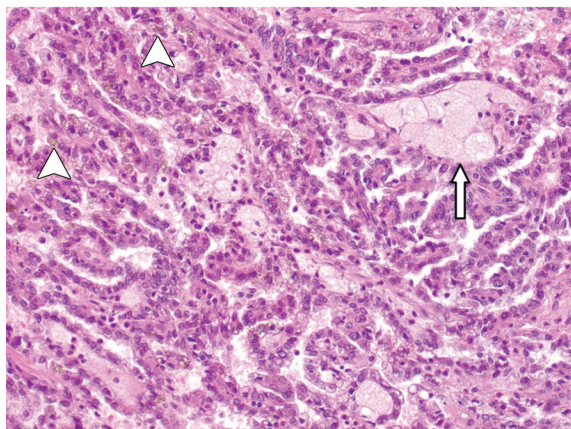
b.
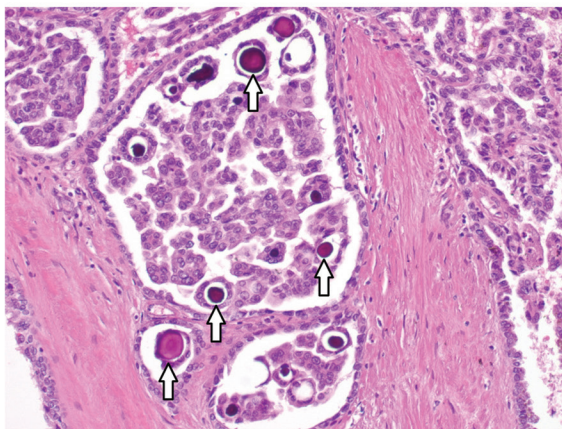
c.

prognostic variables (47). Recent studies have reported finding no significant differences in prognosis between the two subtypes, especially when adjustments to TNM (tumor-node-metastasis) category and nuclear grade are made (48,49). Metastases occur in approximately 7% of cases, mostly to the liver and lungs (11). Around 86% are stage T1 or T2 at presentation, and renal vein invasion is observed in fewer than 5% of cases. A few cases of lymph node and distant metastases have been described (15).

Macroscopically, they are solid, well-circumscribed, tan-brown tumors with a mildly lobulated surface (15). The mean tumor size is 7.2 cm, which is larger than the other subtypes encountered (35). Histopathologically, it has been postulated that these tumors arise from the intercalated cells of the renal cortex and are comprised of variable amounts of cells with clear or eosinophilic cytoplasm arranged in sheet-like architecture along vascular septa (Fig 6) (11). Chromophobe RCCs share the same origin as oncocytomas and have overlapping histologic and imaging features (50).

At MR imaging, no specific features are associated with chromophobe tumors, but they tend to be well-circumscribed and homogeneous. The signal intensity of chromophobe RCCs on

T2-weighted images varies considerably; however, they tend to show intermediate to low signal intensity on T2-weighted images (16). Cystic change and central necrosis are uncommon features, even in larger tumors (11).

The enhancement pattern of these lesions on gadolinium-enhanced images seems to be "intermediate"; that is, less than in clear cell RCCs and greater than in papillary carcinomas (51). Chromophobe RCCs may show a central stellate scar (30%–40% of cases) (50) and spoke-wheel enhancement, but these are not specific features, as oncocytomas may have similar characteristics (Fig 7). Segmental enhancement inversion, another nonspecific feature and also seen in oncocytomas, has been described as areas that enhance avidly after administration of gadolinium contrast material on early phase images but enhance less on more delayed images, whereas other areas that appear hypovascular on early phase images show progressive enhancement on more delayed images (3,52). Calcifications may be present in up to 38% of cases, while perinephric invasion and vascular involvement are rare.

Chromophobe carcinomas have been reported to have lower ADCs than clear cell RCCs (32,53). Conflicting results are seen when
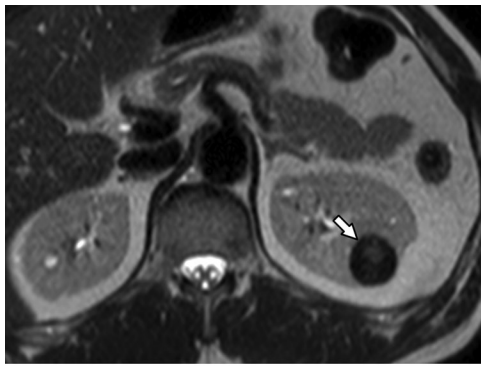
Figure 5. Papillary RCC in a 47-year-old man with a renal lesion corresponding to that in Figure 4 seen at chest computed tomography (CT). **(a)** Axial T2-weighted image shows a 2.8-cm hypointense renal mass (arrow). **(b, c)** Axial in-phase **(b)** and opposed-phase **(c)** T1-weighted images show a drop in signal intensity on the in-phase image (arrow in **b**) compared with that on the opposed-phase image (arrow in **c**), consistent with hemosiderin. **(d, e)** Corticomedullary phase **(d)** and nephrographic phase **(e)** axial 3D fat-saturated SPGR T1-weighted images show mild enhancement (arrow).
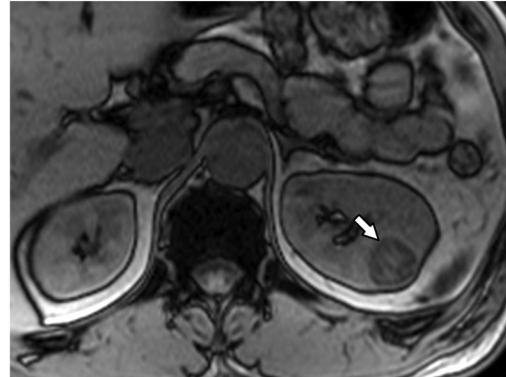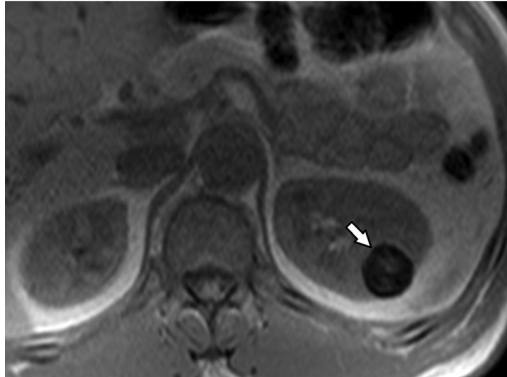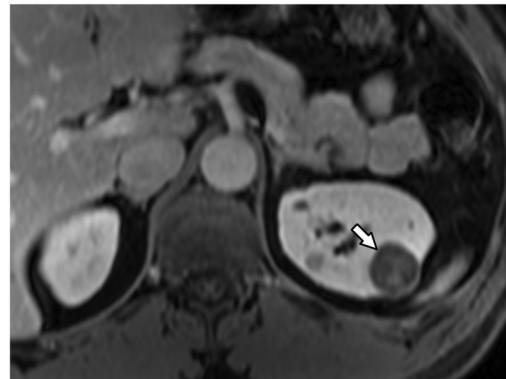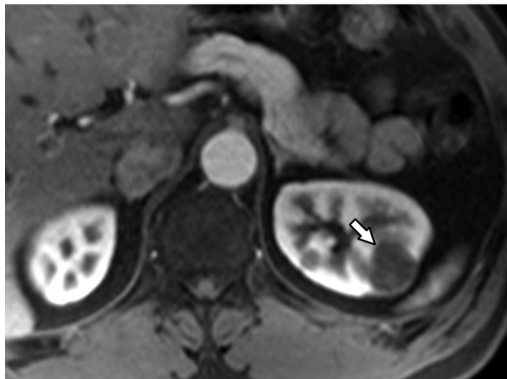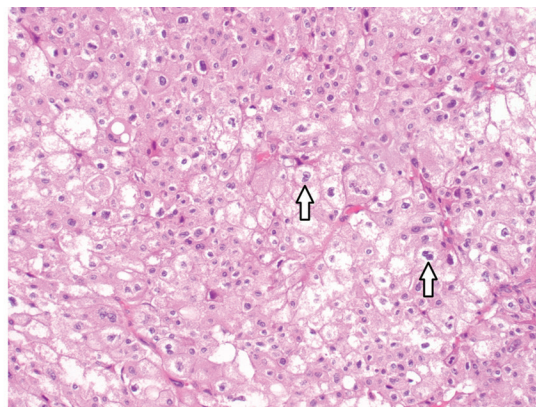

Figure 6. Chromophobe RCC. **(a)** Photograph of a sectioned gross specimen shows a chromophobe RCC (tan-brown appearance). **(b)** High-power photomicrograph shows classic nuclear features of chromophobe RCC including prominent nuclear membranes, nuclear enlargement, hyperchromasia, binucleation (arrows), irregular nuclear contours, and perinuclear clearing (halos). (H-E stain; original magnification, ×100.)

Figure 7. Chromophobe RCC corresponding to that in Figure 6 in a 47-year-old woman. **(a)** Axial T2-weighted image shows a 4.8-cm predominantly hypointense renal mass (arrow). **(b)** Axial contrast-enhanced excretory phase 3D fat-saturated SPGR T1-weighted image shows moderate heterogeneous enhancement with a central scar (arrow). **(c)** Axial diffusion-weighted image (b = 800 sec/mm^2) shows restricted diffusion (arrow). **(d, e)** Axial in-phase **(d)** and opposed-phase **(e)** T1-weighted images show no change in signal intensity (arrow).
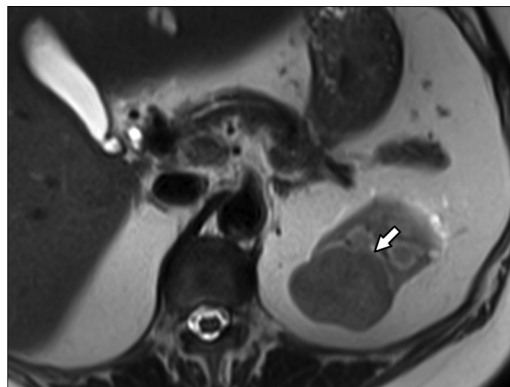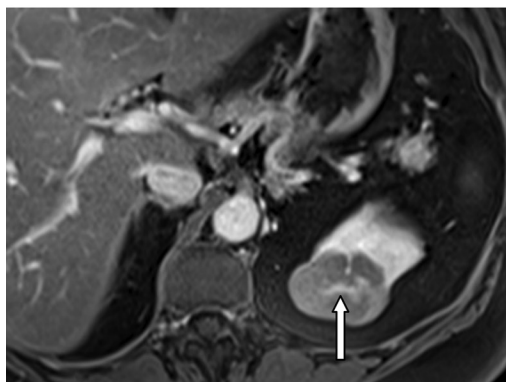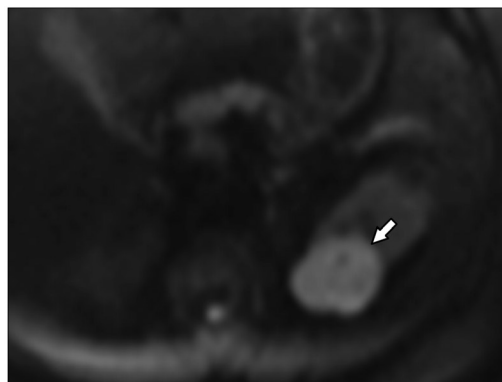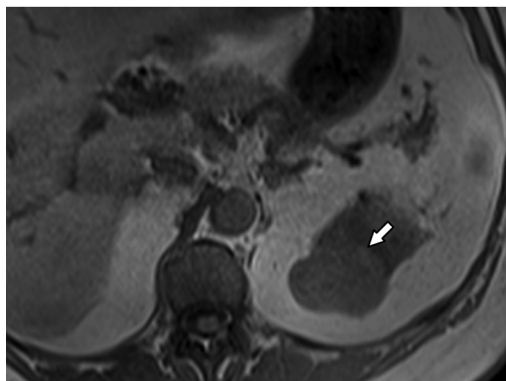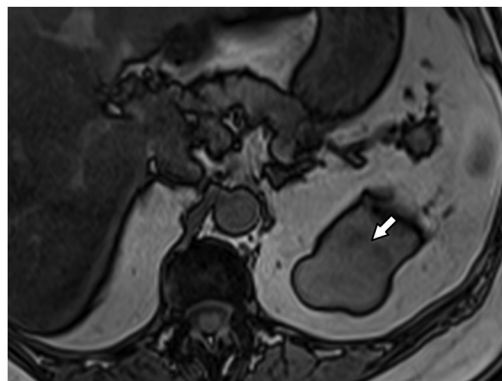
comparing ADCs in papillary versus chromophobe RCCs: Choi et al (9) and Wang et al (32) found that papillary RCCs had lower ADCs than chromophobe RCCs, while Yu et al (54) found the opposite. Given the conflicting results, DWI likely has limitations in distinguishing between the various subtypes, similar to the situation with liver lesions, where DWI has limitations in distinguishing between the various solid benign and malignant hepatic masses (55).

Benign Lesions

Angiomyolipoma
AML is one of the most commonly encountered benign solid renal tumors (56,57). These lesions occur most frequently in the 4th–6th decades with increased prevalence in women (57). They are now regarded as part of the family of perivascular epithelioid cell (PEComa) tumors and comprise a heterogeneous group of tumors with variable pathologic, imaging, and clinical features (56,58). AMLs are typically composed of variable amounts of dysmorphic blood vessels, smooth muscle components, and mature adipose tissue (Fig 8) (56,58).

Approximately 80% of AMLs are sporadic and incidental; the remaining 20% are associated with tuberous sclerosis complex and may also be associated with lymphangioleiomyomatosis (56). An example of an AML associated with tuberous sclerosis complex is the epithelioid AML (58), a rare type that contains few or no fat cells (56,58).
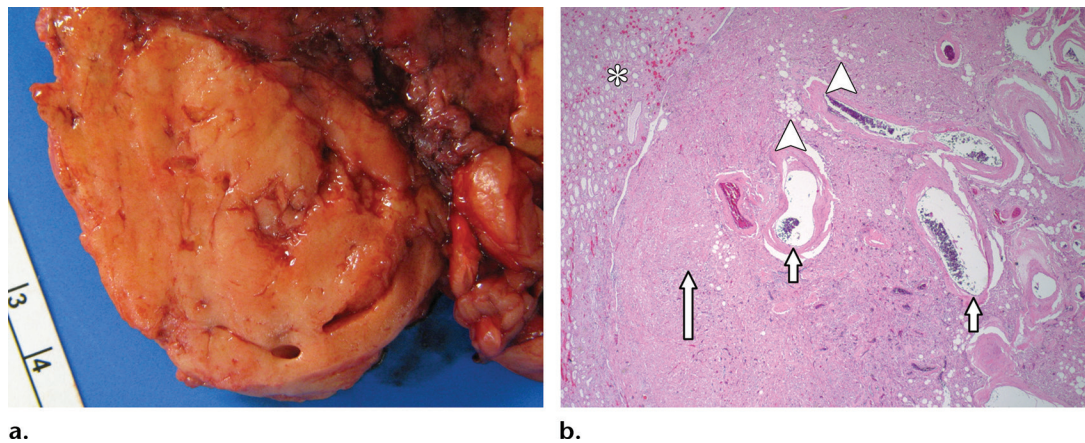
a.   **b.**

Figure 8. AML. **(a)** Photograph of a sectioned gross specimen shows an AML. **(b)** Low-power photomicrograph shows normal renal parenchyma (∗). The tumor is composed of three components: fat (arrowheads), thick-walled abnormal vessels (small arrows), and bland spindle cells reminiscent of smooth muscle (large arrow). (H-E stain; original magnification, ×40.)

Epithelioid AMLs may demonstrate aggressive clinical behavior (56,58,59), including extension into the vena cava and metastasis (59).

In the 10% of cases in which AMLs are larger than 4 cm, there is increased risk for potentially life-threatening hemorrhage (Wunderlich syndrome) (23,60). With tumor growth, there is an increase in blood flow entering the AML and causing vessel dilatation and pseudoaneurysm formation and enlargement (61). In addition, it has been found that ruptured tumors had large pseudoaneurysms (>5 mm), suggesting that those seen at angiography are hemorrhagic pseudoaneurysms (61).

Rarely, large AMLs can be considerably exophytic and difficult to differentiate from perinephric liposarcomas (62). Features that help suggest an exophytic AML include a well-marginated lesion, a sharp renal parenchymal defect suggesting renal origin, and the presence of enlarged vessels (62,63).

At imaging, AMLs are classified as classic AML and lipid-poor AML, depending on their appearance. In the radiology literature, lipid-poor AML has also been described as *fat-poor AML*, *minimal-fat AML*, and *AML without visible fat* at CT and MR imaging. Classic AMLs are easier to diagnose, as they manifest with the pathologic hallmark feature of abundant macroscopic fat and thus are readily identified at cross-sectional imaging (56,57). However, it may be difficult to distinguish lipid-poor AMLs from RCCs. In ambiguous cases, in which other imaging modalities show nonspecific features, multiparametric MR imaging may be helpful.

At MR imaging, classic AMLs demonstrate high T1 signal intensity because of their fat content. The presence of macroscopic fat can be appreciated as suppression of signal intensity on frequency-selective fat-saturated images and as india ink artifact on opposed-phase images (Fig 9) (56,64). India ink artifact occurs due to the presence of fat and water protons within the same imaging voxel, resulting in signal loss and seen as a sharp black line at fat-water interfaces (64). The signal intensity on T2-weighted images varies depending on the amount of fat content in the lesion. AMLs with high fat content appear relatively hyperintense on T2-weighted images, while lesions with lower fat content appear hypointense (23,65).

Benign lesions, such as classic AMLs and benign cystic lesions (66), may display the angular interface sign with the renal parenchyma because of their exophytic growth (67). However, in the study by Takahashi et al (67), the angular interface sign was found in only two of the 24 AMLs without visible fat and was also seen in three of 148 RCCs. Some AMLs expand broadly into the perinephric space with a narrow base of attachment to the kidney (3), resulting in a "mushroom shape appearance." Case reports have described RCCs with macroscopic fat associated with calcification or ossification (68,69). MR imaging may not show the calcifications as well as CT, but fortunately these lesions are rare. In addition, RCCs can engulf perinephric and renal sinus fat, mimicking AMLs.

Lipid-poor AMLs account for 5% of AMLs and are typically reported to be small, with an average diameter of 3 cm (57,70). A lipid-poor AML is pathologically described as an AML containing no more than 25% fat cells per high-power field (56–58). Lipid-poor AMLs are composed nearly entirely of smooth muscle and disordered vascular components (Fig 10) (56).

Figure 9. AML corresponding to that in Figure 8 in a 39-year-old woman. **(a)** Axial T2-weighted image shows a 6.8-cm hyperintense renal mass (arrow). **(b)** Axial fat-suppressed 3D SPGR T1-weighted image shows low signal intensity (arrow). **(c)** Axial contrast-enhanced corticomedullary phase 3D fat-saturated SPGR T1-weighted image shows heterogeneous enhancement (arrow). **(d, e)** Axial in-phase **(d)** and opposed-phase **(e)** T1-weighted images show india ink artifact (arrows) on the opposed-phase image, consistent with macroscopic fat.
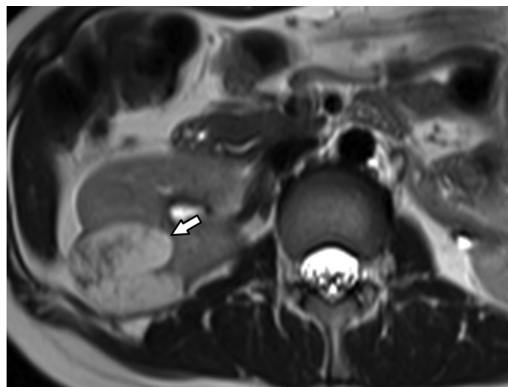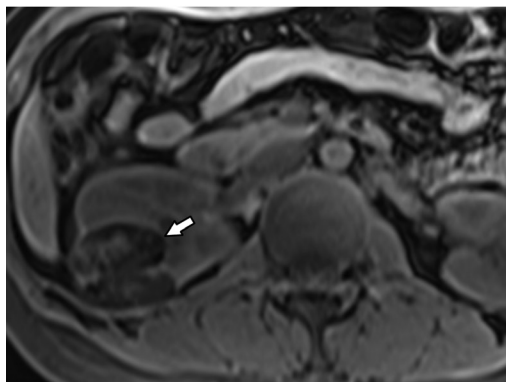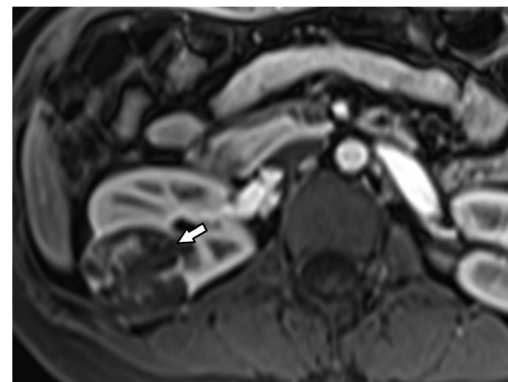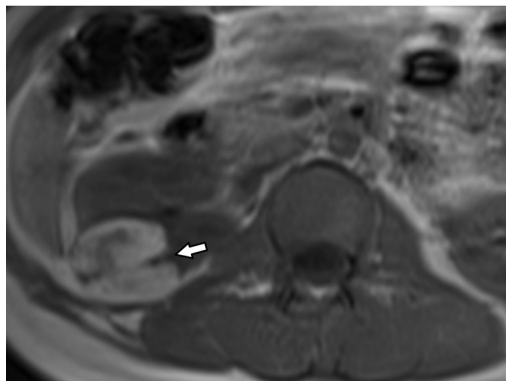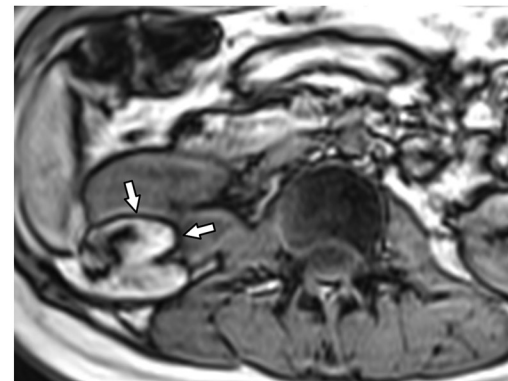
At MR imaging, these lesions are homogeneous and show low signal intensity on T2-weighted images (Fig 11) due to the presence of abundant smooth muscle and high signal intensity on T1-weighted images. The enhancement pattern of lipid-poor AMLs is typically early intense enhancement with subsequent washout (65,71), although it can be variable. Lipid-poor AMLs may appear as an exophytic (67) non-round lesion without a capsule (72). Lipid-poor AMLs may show a drop in signal intensity on opposed-phase images when compared with in-phase images (57,63–65).

While fat suppression sequences are mostly useful for detection of macroscopic fat, they may enhance the ability to demonstrate small amounts of fat when subtle changes in signal intensity between the lesion and a chosen reference point (eg, the spleen or kidney) are analyzed using ratios (58). Lipid-poor AML has been shown to have a higher signal intensity index (calculated as $[SI_{in\text{-}phase} - SI_{opposed\text{-}phase}]/SI_{in\text{-}phase} \times 100$) and lower tumor-to-spleen signal intensity ratio at double-echo chemical shift imaging (21). Also, lipid-poor AMLs demonstrate a high signal intensity ratio between early and delayed postcontrast images (71).

AMLs show restricted diffusion with a corresponding low ADC, but restricted diffusion is not specific for AML (3). One study suggested that clear cell RCC had more heterogeneous signal intensity at DWI, with several peaks in the

a.

b.
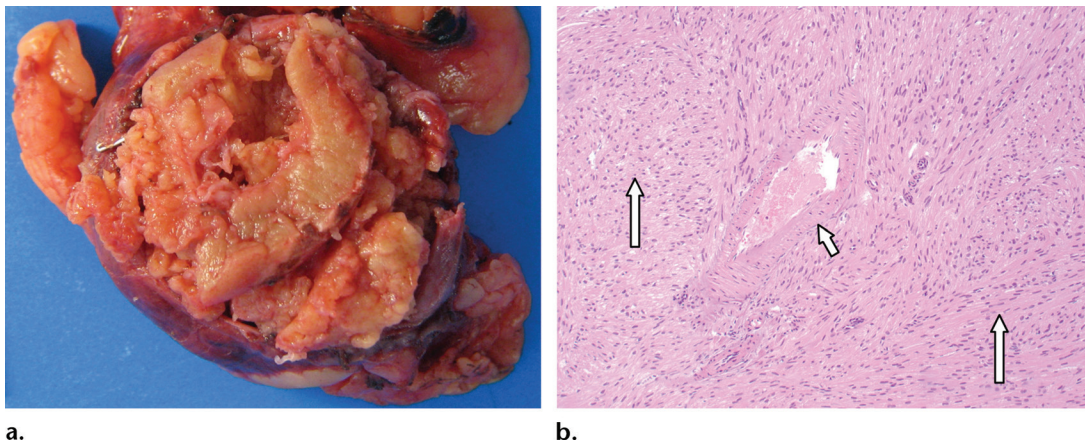
Figure 10. Lipid-poor AML. **(a)** Photograph of a sectioned gross specimen shows a lipid-poor AML. **(b)** Low-power photomicrograph shows a tumor almost exclusively composed of pink spindle cells (resembling smooth muscle) (large arrows) and abnormal vessels (small arrow). Virtually no fat is present. (H-E stain; original magnification, ×40.)

a.

b.

c.

d.

e.
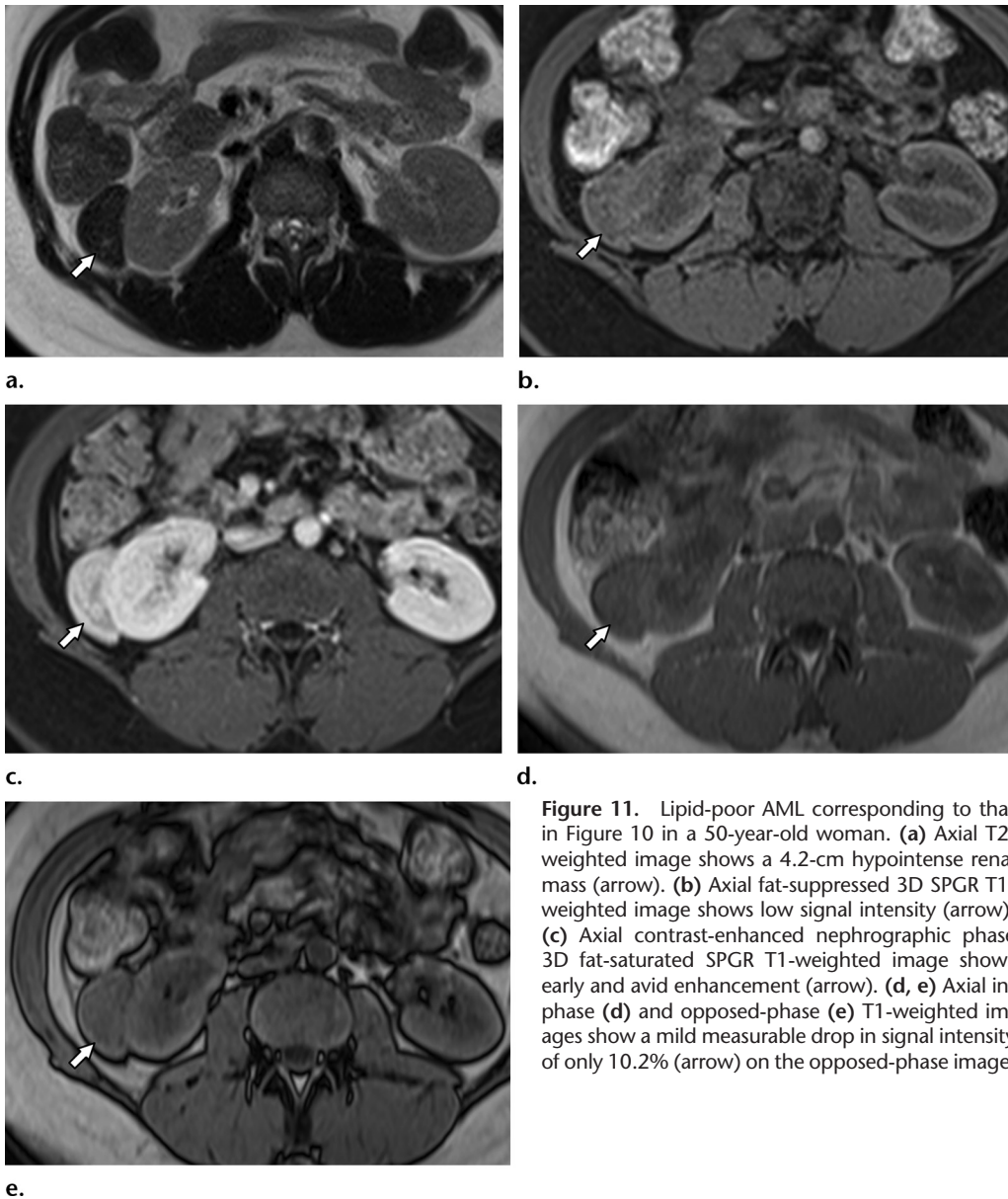
Figure 11. Lipid-poor AML corresponding to that in Figure 10 in a 50-year-old woman. **(a)** Axial T2-weighted image shows a 4.2-cm hypointense renal mass (arrow). **(b)** Axial fat-suppressed 3D SPGR T1-weighted image shows low signal intensity (arrow). **(c)** Axial contrast-enhanced nephrographic phase 3D fat-saturated SPGR T1-weighted image shows early and avid enhancement (arrow). **(d, e)** Axial in-phase **(d)** and opposed-phase **(e)** T1-weighted images show a mild measurable drop in signal intensity of only 10.2% (arrow) on the opposed-phase image.
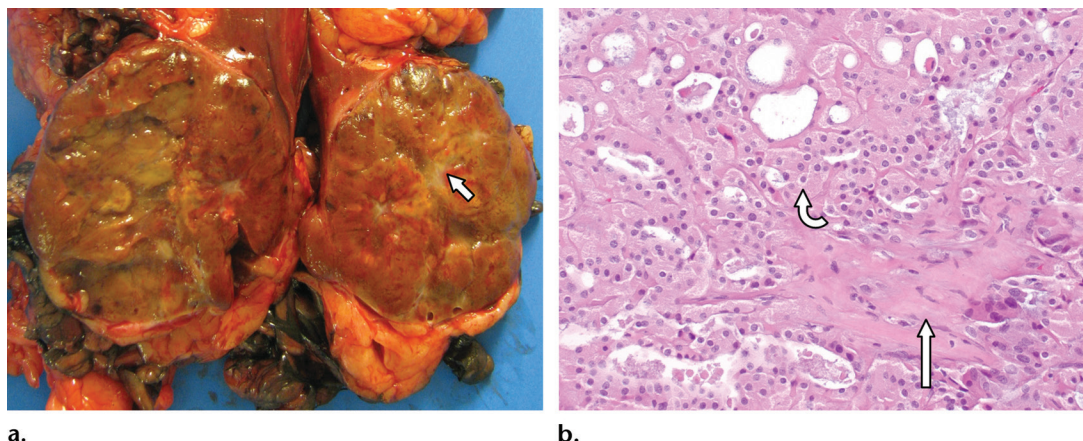
Figure 12.   Oncocytoma. **(a)** Photograph of a sectioned gross specimen shows an oncocytoma with a central scar (arrow). **(b)** Higher-power photomicrograph shows round and uniform tumor cells with abundant granular and eosinophilic cytoplasm (curved arrow). The cells are invested by the myxohyaline stroma (straight arrow). (H-E stain; original magnification, ×100.)

ADC histogram, compared to four of five AMLs with minimal fat, which had homogeneous signal intensity at DWI with a single prominent peak (73). Larger series are necessary to confirm these findings.

Oncocytoma

Oncocytomas account for 3%–7% of solid renal masses and are considered benign neoplasms (50). The peak incidence of these lesions is in the 7th decade, with a higher prevalence in men (57). Oncocytomas share the same origin as chromophobe RCCs and therefore have overlapping histologic and imaging features (50). Chromophobe RCCs and oncocytomas are often referred to as "oncocytic neoplasms."

Macroscopically, these tumors are tan or mahogany brown, fairly homogeneous, and usually encapsulated (6). Histopathologically, they are organized with acini and nests of large polygonal cells containing eosinophilic cytoplasm rich in mitochondria (Fig 12) (57). A central stellate scar composed of fibrous or hyalinized connective tissue with compressed blood vessels may be observed in up to 54% of cases (53).

Oncocytomas have variable and nonspecific MR imaging features that overlap with characteristics of RCCs and make it difficult to properly diagnose them preoperatively. Most commonly, they appear as a peripheral mostly or completely well-circumscribed lesion with avid enhancement (3,53). They show low signal intensity on T1-weighted images and high signal intensity on T2-weighted images.

In about one-half of oncocytomas, a well-defined capsule of low signal intensity may be seen, but it is not specific and can also be seen in RCCs. The central stellate scar, when present (50%–61% of cases) (50), appears as a stellate

area of low signal intensity on T1-weighted images and high signal intensity on T2-weighted images and may show a stellate or spoke-wheel pattern of enhancement (Fig 13). The appearance of a central scar as seen in oncocytomas can also be seen in RCCs, including the chromophobe subtype, from necrosis or cystic changes (7,53).

Although not specific, segmental enhancement inversion, related to the changes in the pattern of heterogeneous enhancement within the mass, may be observed in oncocytomas but may also be seen in RCC (particularly the chromophobe subtype) (50,53). Like chromophobe RCCs, oncocytomas usually do not manifest with perinephric fat invasion or renal vein invasion (53). DWI has limitations in diagnosing oncocytomas. Although some studies have shown that oncocytomas have higher ADCs compared with RCCs (74), others have shown that similar ADCs can be seen with oncocytomas and clear cell RCC (30).

A possible distinguishing feature for oncocytomas examined in one study was the percentage washout value (mean percentage of contrast material excreted at the end of the delayed phase). Oncocytomas were associated with the highest (>50%) percentage washout value, followed by clear cell RCC, chromophobe RCC, and papillary RCC, none of which displayed a washout value greater than 50% besides oncocytomas (75). Also, only oncocytomas demonstrated mean arterial phase enhancement of greater than 500%, but additional studies with more patients are needed to confirm these results (75).

Diagnostic Approach

The main MR imaging characteristics of the lesions described in this article are summarized in Table 3.
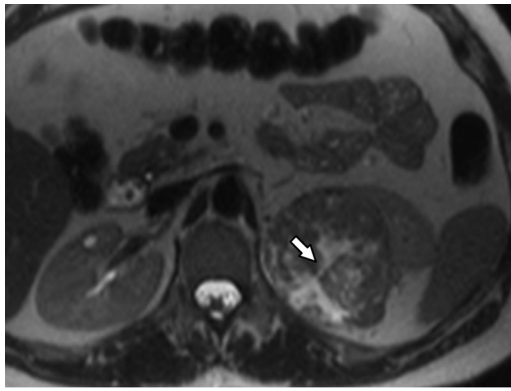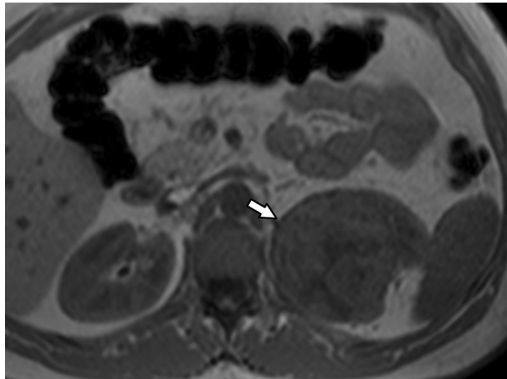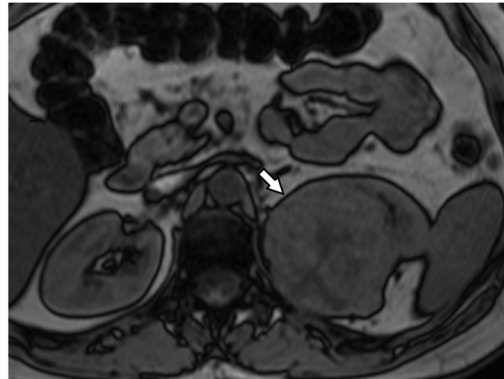
Figure 13. Oncocytoma corresponding to that in Figure 12 in a 45-year-old woman. **(a)** Axial T2-weighted image shows a 7.1-cm heterogeneous renal mass with a hyperintense central portion (arrow). **(b)** Axial fat-suppressed 3D SPGR T1-weighted image shows a heterogeneous renal mass with a hypointense central portion (arrow). **(c)** Axial contrast-enhanced 3D SPGR T1-weighted image shows heterogeneous enhancement with a hypointense central portion (arrow). **(d, e)** Axial in-phase **(d)** and opposed-phase **(e)** T1-weighted images show no change in signal intensity (arrow).

The following considerations should be taken into account when trying to diagnose a solid renal mass using multiparametric MR imaging. If a renal mass demonstrates low T2 signal intensity, the differential diagnosis includes papillary RCC, lipid-poor AML, hemorrhagic cyst, and rarely metanephric adenoma. If low T2 signal intensity is seen with enhancement, hemorrhagic cyst can be excluded since it should not enhance. If the low T2 signal intensity mass is hypovascular with progressive enhancement and shows signal intensity drop on in-phase images relative to opposed-phase images, suggesting hemosiderin, then the lesion is most likely a papillary RCC. On the other hand, if the lesion has low T2 signal intensity and shows avid or moderate enhancement and signal intensity drop on opposed-phase images, because of microscopic fat, the lesion is suggestive of a lipid-poor AML.

If a solid renal mass has high signal intensity on T2-weighted images and shows hypervascularity and signal intensity drop because of microscopic fat on opposed-phase images, the differential diagnosis mostly includes clear cell RCC and classic AML. For differentiating them, frequency-selective fat-suppressed images should be evaluated. If the lesion has any areas demonstrating macroscopic fat suppression, the lesion represents a classic AML. Classic AMLs may also demonstrate india ink artifact on opposed-phase images and only exceedingly rarely contain central necrosis. Central necrosis is more often found in large clear cell RCCs.

DWI can be helpful in renal imaging, especially in detection of RCC and other solid masses and in

Table 3: Key Multiparametric MR Imaging Features of Solid Renal Masses

Renal Lesion	Key MR Imaging Features
Clear cell RCC	High SI on T2WI + microscopic fat + hypervascularity
Papillary RCC	Low SI on T2WI + hypovascularity + may contain hemosiderin
Chromophobe RCC	No definitive MR imaging features → pathologic diagnosis
Classic AML	Macroscopic fat
Lipid-poor AML	Low SI on T2WI + avid early enhancement + may contain microscopic fat
Oncocytoma	No definitive MR imaging features → pathologic diagnosis

Note.—SI = signal intensity, T2WI = T2-weighted images.

characterizing abscesses. In general, lesions with restricted diffusion suggest malignancy or infection, but there is potential overlap with solid benign lesions including oncocytomas and lipid-poor AMLs. Some studies have found DWI to be useful in identification of clear cell RCC as solid renal masses with higher ADC; however, not all studies corroborate this finding. Application of DWI on an individual patient basis is limited, as there is significant overlap of ADCs between different subtypes of RCC in the published literature.

Chromophobe carcinoma and oncocytoma originate from a common progenitor cell in the kidney and therefore have overlapping histologic and imaging features. A central stellate scar and segmental enhancement inversion have been found in both of these lesions; thus, these imaging findings will not assist in their differentiation. If a renal mass manifests with any of these nonspecific imaging features, surgical resection, biopsy, or follow-up imaging would be required, based on consultation with the urologist.

Conclusion

Recognition of the most important imaging features of solid renal masses may assist in their proper diagnosis and management. Multiparametric MR imaging as a noninvasive imaging method provides critical information that can help in differentiation of the most common solid renal masses, including the common RCC subtypes and AMLs, and as a result may assist in selecting the most appropriate management and follow-up of these lesions.

References

1. Volpe A, Panzarella T, Rendon RA, Haider MA, Kondylis FI, Jewett MA. The natural history of incidentally detected small renal masses. Cancer 2004;100(4):738–745.
2. Cornelis F, Tricaud E, Lasserre AS, et al. Routinely performed multiparametric magnetic resonance imaging helps to differentiate common subtypes of renal tumours. Eur Radiol 2014;24(5):1068–1080.
3. Allen BC, Tirman P, Jennings Clingan M, Manny J, Del Gaizo AJ, Leyendecker JR. Characterizing solid renal neoplasms with MRI in adults. Abdom Imaging 2014;39(2):358–387.
4. Motzer RJ, Agarwal N, Beard C, et al. Kidney cancer. J Natl Compr Canc Netw 2011;9(9):960–977.
5. Cheville JC, Lohse CM, Zincke H, Weaver AL, Blute ML. Comparisons of outcome and prognostic features among histologic subtypes of renal cell carcinoma. Am J Surg Pathol 2003;27(5):612–624.
6. Perez-Ordonez B, Hamed G, Campbell S, et al. Renal oncocytoma: a clinicopathologic study of 70 cases. Am J Surg Pathol 1997;21(8):871–883.
7. Amin MB, Crotty TB, Tickoo SK, Farrow GM. Renal oncocytoma: a reappraisal of morphologic features with clinicopathologic findings in 80 cases. Am J Surg Pathol 1997;21(1):1–12.
8. Ramamurthy NK, Moosavi B, McInnes MD, Flood TA, Schieda N. Multiparametric MRI of solid renal masses: pearls and pitfalls. Clin Radiol 2015;70(3):304–316.
9. Choi YA, Kim CK, Park SY, Cho SW, Park BK. Subtype differentiation of renal cell carcinoma using diffusion-weighted and blood oxygenation level-dependent MRI. AJR Am J Roentgenol 2014;203(1):W78–W84.
10. Lopez-Beltran A, Scarpelli M, Montironi R, Kirkali Z. 2004 WHO classification of the renal tumors of the adults. Eur Urol 2006;49(5):798–805.
11. Gurel S, Narra V, Elsayes KM, Siegel CL, Chen ZE, Brown JJ. Subtypes of renal cell carcinoma: MRI and pathological features. Diagn Interv Radiol 2013;19(4):304–311.
12. Hötker AM, Karlo CA, Zheng J, et al. Clear cell renal cell carcinoma: associations between CT features and patient survival. AJR Am J Roentgenol 2016;206(5):1023–1030.
13. Moch H, Gasser T, Amin MB, Torhorst J, Sauter G, Mihatsch MJ. Prognostic utility of the recently recommended histologic classification and revised TNM staging system of renal cell carcinoma: a Swiss experience with 588 tumors. Cancer 2000;89(3):604–614.
14. Polascik TJ, Bostwick DG, Cairns P. Molecular genetics and histopathologic features of adult distal nephron tumors. Urology 2002;60(6):941–946.
15. Prasad SR, Humphrey PA, Catena JR, et al. Common and uncommon histologic subtypes of renal cell carcinoma: imaging spectrum with pathologic correlation. RadioGraphics 2006;26(6):1795–1806; discussion 1806–1810.
16. Muglia VF, Prando A. Renal cell carcinoma: histological classification and correlation with imaging findings. Radiol Bras 2015;48(3):166–174.
17. Fuhrman SA, Lasky LC, Limas C. Prognostic significance of morphologic parameters in renal cell carcinoma. Am J Surg Pathol 1982;6(7):655–663.
18. Lohse CM, Blute ML, Zincke H, Weaver AL, Cheville JC. Comparison of standardized and nonstandardized nuclear grade of renal cell carcinoma to predict outcome among 2,042 patients. Am J Clin Pathol 2002;118(6):877–886.

19. Delahunt B. Advances and controversies in grading and staging of renal cell carcinoma. Mod Pathol 2009;22(suppl 2):S24–S36.
20. Novara G, Martignoni G, Artibani W, Ficarra V. Grading systems in renal cell carcinoma. J Urol 2007;177(2):430–436.
21. Oliva MR, Glickman JN, Zou KH, et al. Renal cell carcinoma: T1 and T2 signal intensity characteristics of papillary and clear cell types correlated with pathology. AJR Am J Roentgenol 2009;192(6):1524–1530.
22. Hötker AM, Mazaheri Y, Wibmer A, et al. Differentiation of clear cell renal cell carcinoma from other renal cortical tumors by use of a quantitative multiparametric MRI approach. AJR Am J Roentgenol 2017;208(3):W85–W91.
23. Pedrosa I, Sun MR, Spencer M, et al. MR imaging of renal masses: correlation with findings at surgery and pathologic analysis. RadioGraphics 2008;28(4):985–1003.
24. Karlo CA, Donati OF, Burger IA, et al. MR imaging of renal cortical tumours: qualitative and quantitative chemical shift imaging parameters. Eur Radiol 2013;23(6):1738–1744.
25. Kuthi L, Jenei A, Hajdu A, et al. Prognostic factors for renal cell carcinoma subtypes diagnosed according to the 2016 WHO Renal Tumor Classification: a study involving 928 patients. Pathol Oncol Res 2017;23(3):689–698.
26. Bissada NK, Yakout HH, Babanouri A, et al. Long-term experience with management of renal cell carcinoma involving the inferior vena cava. Urology 2003;61(1):89–92.
27. Roy C Sr, El Ghali S, Buy X, et al. Significance of the pseudo-capsule on MRI of renal neoplasms and its potential application for local staging: a retrospective study. AJR Am J Roentgenol 2005;184(1):113–120.
28. Cornelis F, Tricaud E, Lasserre AS, et al. Multiparametric magnetic resonance imaging for the differentiation of low and high grade clear cell renal carcinoma. Eur Radiol 2015;25(1):24–31.
29. Parada Villavicencio C, Mc Carthy RJ, Miller FH. Can diffusion-weighted magnetic resonance imaging of clear cell renal carcinoma predict low from high nuclear grade tumors. Abdom Radiol (NY) 2017;42(4):1241–1249.
30. Hötker AM, Mazaheri Y, Wibmer A, et al. Use of DWI in the differentiation of renal cortical tumors. AJR Am J Roentgenol 2016;206(1):100–105.
31. Goyal A, Sharma R, Bhalla AS, et al. Diffusion-weighted MRI in renal cell carcinoma: a surrogate marker for predicting nuclear grade and histological subtype. Acta Radiol 2012;53(3):349–358.
32. Wang H, Cheng L, Zhang X, et al. Renal cell carcinoma: diffusion-weighted MR imaging for subtype differentiation at 3.0 T. Radiology 2010;257(1):135–143.
33. Sandrasegaran K, Sundaram CP, Ramaswamy R, et al. Usefulness of diffusion-weighted imaging in the evaluation of renal masses. AJR Am J Roentgenol 2010;194(2):438–445.
34. Hoffmann NE, Gillett MD, Cheville JC, Lohse CM, Leibovich BC, Blute ML. Differences in organ system of distant metastasis by renal cell carcinoma subtype. J Urol 2008;179(2):474–477.
35. Amin MB, Amin MB, Tamboli P, et al. Prognostic impact of histologic subtyping of adult renal epithelial neoplasms: an experience of 405 cases. Am J Surg Pathol 2002;26(3):281–291.
36. Leroy X, Zini L, Leteurtre E, et al. Morphologic subtyping of papillary renal cell carcinoma: correlation with prognosis and differential expression of MUC1 between the two subtypes. Mod Pathol 2002;15(11):1126–1130.
37. Mejean A, Hopirtean V, Bazin JP, et al. Prognostic factors for the survival of patients with papillary renal cell carcinoma: meaning of histological typing and multifocality. J Urol 2003;170(3):764–767.
38. Yoshimitsu K, Kakihara D, Irie H, et al. Papillary renal carcinoma: diagnostic approach by chemical shift gradient-echo and echo-planar MR imaging. J Magn Reson Imaging 2006;23(3):339–344.
39. Doshi AM, Ream JM, Kierans AS, et al. Use of MRI in differentiation of papillary renal cell carcinoma subtypes: qualitative and quantitative analysis. AJR Am J Roentgenol 2016;206(3):566–572.
40. Delahunt B, Eble JN. Papillary renal cell carcinoma: a clinicopathologic and immunohistochemical study of 105 tumors. Mod Pathol 1997;10(6):537–544.
41. Delahunt B, Eble JN, McCredie MR, Bethwaite PB, Stewart JH, Bilous AM. Morphologic typing of papillary renal cell carcinoma: comparison of growth kinetics and patient survival in 66 cases. Hum Pathol 2001;32(6):590–595.
42. Yamada T, Endo M, Tsuboi M, et al. Differentiation of pathologic subtypes of papillary renal cell carcinoma on CT. AJR Am J Roentgenol 2008;191(5):1559–1563.
43. Rosenkrantz AB, Sekhar A, Genega EM, et al. Prognostic implications of the magnetic resonance imaging appearance in papillary renal cell carcinoma. Eur Radiol 2013;23(2):579–587.
44. Lin WC, Chen JH. Pitfalls and limitations of diffusion-weighted magnetic resonance imaging in the diagnosis of urinary bladder cancer. Transl Oncol 2015;8(3):217–230.
45. Volpe A, Novara G, Antonelli A, et al. Chromophobe renal cell carcinoma (RCC): oncological outcomes and prognostic factors in a large multicentre series. BJU Int 2012;110(1):76–83.
46. Klatte T, Han KR, Said JW, et al. Pathobiology and prognosis of chromophobe renal cell carcinoma. Urol Oncol 2008;26(6):604–609.
47. Weinzierl EP, Thong AE, McKenney JK, Jeon SH, Chung BI. Relating prognosis in chromophobe renal cell carcinoma to the chromophobe tumor grading system. Korean J Urol 2014;55(4):239–244.
48. Capitanio U, Cloutier V, Zini L, et al. A critical assessment of the prognostic value of clear cell, papillary and chromophobe histological subtypes in renal cell carcinoma: a population-based study. BJU Int 2009;103(11):1496–1500.
49. Cheville JC, Lohse CM, Sukov WR, Thompson RH, Leibovich BC. Chromophobe renal cell carcinoma: the impact of tumor grade on outcome. Am J Surg Pathol 2012;36(6):851–856.
50. Rosenkrantz AB, Hindman N, Fitzgerald EF, Niver BE, Melamed J, Babb JS. MRI features of renal oncocytoma and chromophobe renal cell carcinoma. AJR Am J Roentgenol 2010;195(6):W421–W427.
51. Kay FU, Pedrosa I. Imaging of solid renal masses. Radiol Clin North Am 2017;55(2):243–258.
52. Woo S, Cho JY, Kim SH, et al. Segmental enhancement inversion of small renal oncocytoma: differences in prevalence according to tumor size. AJR Am J Roentgenol 2013;200(5):1054–1059.
53. Galmiche C, Bernhard JC, Yacoub M, Ravaud A, Grenier N, Cornelis F. Is multiparametric MRI useful for differentiating oncocytomas from chromophobe renal cell carcinomas? AJR Am J Roentgenol 2017;208(2):343–350.
54. Yu X, Lin M, Ouyang H, Zhou C, Zhang H. Application of ADC measurement in characterization of renal cell carcinomas with different pathological types and grades by 3.0T diffusion-weighted MRI. Eur J Radiol 2012;81(11):3061–3066.
55. Miller FH, Hammond N, Siddiqi AJ, et al. Utility of diffusion-weighted MRI in distinguishing benign and malignant hepatic lesions. J Magn Reson Imaging 2010;32(1):138–147.
56. Jinzaki M, Silverman SG, Akita H, Nagashima Y, Mikami S, Oya M. Renal angiomyolipoma: a radiological classification and update on recent developments in diagnosis and management. Abdom Imaging 2014;39(3):588–604.
57. Woo S, Cho JY. Imaging findings of common benign renal tumors in the era of small renal masses: differential diagnosis from small renal cell carcinoma—current status and future perspectives. Korean J Radiol 2015;16(1):99–113.
58. Farrell C, Noyes SL, Tourojman M, Lane BR. Renal angiomyolipoma: preoperative identification of atypical fat-poor AML. Curr Urol Rep 2015;16(3):12.
59. Park HK, Zhang S, Wong MK, Kim HL. Clinical presentation of epithelioid angiomyolipoma. Int J Urol 2007;14(1):21–25.
60. Steiner MS, Goldman SM, Fishman EK, Marshall FF. The natural history of renal angiomyolipoma. J Urol 1993;150(6):1782–1786.
61. Yamakado K, Tanaka N, Nakagawa T, Kobayashi S, Yanagawa M, Takeda K. Renal angiomyolipoma: relationships between tumor size, aneurysm formation, and rupture. Radiology 2002;225(1):78–82.
62. Israel GM, Bosniak MA, Slywotzky CM, Rosen RJ. CT differentiation of large exophytic renal angiomyolipomas and perirenal liposarcomas. AJR Am J Roentgenol 2002;179(3):769–773.
63. Israel GM, Bosniak MA. Pitfalls in renal mass evaluation and how to avoid them. RadioGraphics 2008;28(5):1325–1338.

64. Israel GM, Hindman N, Hecht E, Krinsky G. The use of opposed-phase chemical shift MRI in the diagnosis of renal angiomyolipomas. AJR Am J Roentgenol 2005;184(6): 1868–1872.

65. Hindman N, Ngo L, Genega EM, et al. Angiomyolipoma with minimal fat: can it be differentiated from clear cell renal cell carcinoma by using standard MR techniques? Radiology 2012;265(2):468–477.

66. Verma SK, Mitchell DG, Yang R, et al. Exophytic renal masses: angular interface with renal parenchyma for distinguishing benign from malignant lesions at MR imaging. Radiology 2010;255(2):501–507.

67. Takahashi N, Leng S, Kitajima K, et al. Small (< 4 cm) renal masses: differentiation of angiomyolipoma without visible fat from renal cell carcinoma using unenhanced and contrast-enhanced CT. AJR Am J Roentgenol 2015;205(6):1194–1202.

68. Strotzer M, Lehner KB, Becker K. Detection of fat in a renal cell carcinoma mimicking angiomyolipoma. Radiology 1993;188(2):427–428.

69. Hélénon O, Chrétien Y, Paraf F, Melki P, Denys A, Moreau JF. Renal cell carcinoma containing fat: demonstration with CT. Radiology 1993;188(2):429–430.

70. Kim JK, Park SY, Shon JH, Cho KS. Angiomyolipoma with minimal fat: differentiation from renal cell carcinoma at biphasic helical CT. Radiology 2004;230(3):677–684.

71. Sasiwimonphan K, Takahashi N, Leibovich BC, Carter RE, Atwell TD, Kawashima A. Small (<4 cm) renal mass: differentiation of angiomyolipoma without visible fat from renal cell carcinoma utilizing MR imaging. Radiology 2012;263(1):160–168.

72. Sung CK, Kim SH, Woo S, et al. Angiomyolipoma with minimal fat: differentiation of morphological and enhancement features from renal cell carcinoma at CT imaging. Acta Radiol 2016;57(9):1114–1122.

73. Tanaka H, Yoshida S, Fujii Y, et al. Diffusion-weighted magnetic resonance imaging in the differentiation of angiomyolipoma with minimal fat from clear cell renal cell carcinoma. Int J Urol 2011;18(10):727–730.

74. Taouli B, Thakur RK, Mannelli L, et al. Renal lesions: characterization with diffusion-weighted imaging versus contrast-enhanced MR imaging. Radiology 2009;251(2):398–407.

75. Bird VG, Kanagarajah P, Morillo G, et al. Differentiation of oncocytoma and renal cell carcinoma in small renal masses (<4 cm): the role of 4-phase computerized tomography. World J Urol 2011;29(6):787–792.